Inorganic Chemistry
Article
Cite This: Inorg. Chem. XXXX, XXX, XXX−XXX
pubs.acs.org/IC

In Situ Formation of Homogeneous Tellurium Nanodots in Paclitaxel-Loaded MgAl Layered Double Hydroxide Gated Mesoporous Silica Nanoparticles for Synergistic Chemo/PDT/PTT Trimode Combinatorial Therapy

Jia Wen,[†] Kui Yang,[†] Xingcheng Ding,[‡] Hongjuan Li,[†] Yongqian Xu,[†] Fengyu Liu,*[,§] and Shiguo Sun*[,†]

[†]Shaanxi Key Laboratory of Natural Products & Chemical Biology, College of Chemistry & Pharmacy, Northwest A&F University, Yangling, Shaanxi 712100, People's Republic of China

[‡]Zhejiang Runtu Co., Ltd, Shangyu, Zhejiang, People's Republic of China

[§]State Key Laboratory of Fine Chemicals, School of Chemistry, Dalian University of Technology, No.2 linggong Road, Ganjingzi District, Dalian 116023, China

Supporting Information

ABSTRACT: A folic acid (FA) functional drug delivery system (MT@L-PTX@FA) based on in situ formation of tellurium nanodots (Te NDs) in paclitaxel (PTX)-loaded MgAl layered double hydroxide (LDHs) gated mesoporous silica nanoparticles (MSNs) has been designed and fabricated for targeted chemo/PDT/PTT trimode combinatorial therapy. X-ray diffraction (XRD), X-ray photoelectron spectroscopy (XPS), scanning electron microscopy (SEM), high-resolution transmission electron microscopy (HRTEM), N_2 adsorption−desorption, Fourier transform infrared (FT-IR) spectra, and UV−vis spectra were used to demonstrate the successful fabrication of MT@L-PTX@FA. In particular, the in situ generated Te NDs showed a homogeneous ultrasmall size. Reactive oxygen species (ROS) generation, photothermal effects, and photostability evaluations indicated that the in situ generated homogeneous Te NDs could serve as the photo-therapeutic agent, converting the photon energy to ROS and heat under near-infrared (NIR) irradiation efficiently. The drug-release test revealed that MT@L-PTX@FA showed an apparent sustained release character in a pH-sensitive manner. In addition, cell imaging experiments demonstrated that MT@L-PTX@FA could selectively enter into cancer cells owing to the function of FA and release of PTX efficiently for chemotherapy for the reason that the low intracellular pH would dissolve MgAl LDHs to Mg^{2+} and Al^{3+}. Cytotoxicity tests also indicated that MT@L-PTX@FA exhibited enhanced therapeutic effect in cancer cells under NIR irradiation, benefiting from the synergy based on targeted chemo/PDT/PTT trimode combinatorial therapy. The preliminary results reported here will shed new light on the future design and applications of nanosystems for synergistic combinatorial therapy.

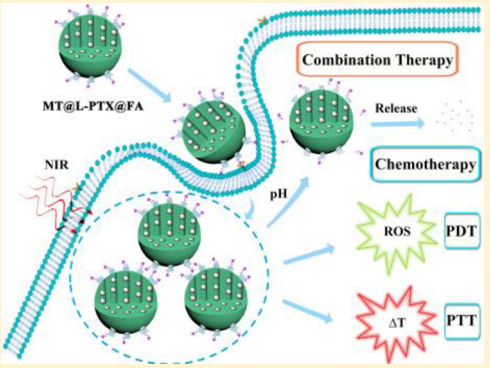

INTRODUCTION

Chemotherapy still remains one of the best means to cure cancer.[1−5] However, after continuous treatment with a single chemotherapeutic modality, cancer cells are able to bypass the pathways affected by anticancer drugs and generate drug resistance, leading to cancer recurrence and even the failure of chemotherapy.[6−8] This deficiency has inspired the improvement of other therapeutic modalities.[9−12] Among them, phototherapies such as photodynamic therapy (PDT) and photothermal therapy (PTT), where the process mainly includes delivery of phototherapeutic agents to tumors and subsequently irradiation of the treated tumor site with specific light,[13−15] have gained considerable attention in recent years due to their high tumor ablation efficiency, excellent spatial resolution, and minimal side effects on normal tissue.[16−18] Some researchers have utilized the combination of PDT or PTT with chemotherapy to overcome the limitations of single chemotherapy, gaining synergistic effects and reducing the therapeutic doses of both phototherapeutic agents and anticancer drugs, resulting in minimized side effects.[19−23] Unfortunately, the outcome remains suboptimal and unsatisfactory for completely curing cancer. Therefore, to further enhance the therapeutic efficiency as well as minimize side effects, triple or even more modes of combinatorial therapy are highly desired.

Tellurium (Te), a narrow band gap semiconductor widely used in electrochemistry and optoelectronics applications,[24−26]

Received: October 4, 2018

DOI: 10.1021/acs.inorgchem.8b02821
Inorg. Chem. XXXX, XXX, XXX−XXX

Scheme 1. Schematic Illustration of (a) L-PTX Preparation, (b) MT@L-PTX@FA Preparation, and (c) Intracellular Tri-Mode Combination Therapy of MT@L-PTX@FA

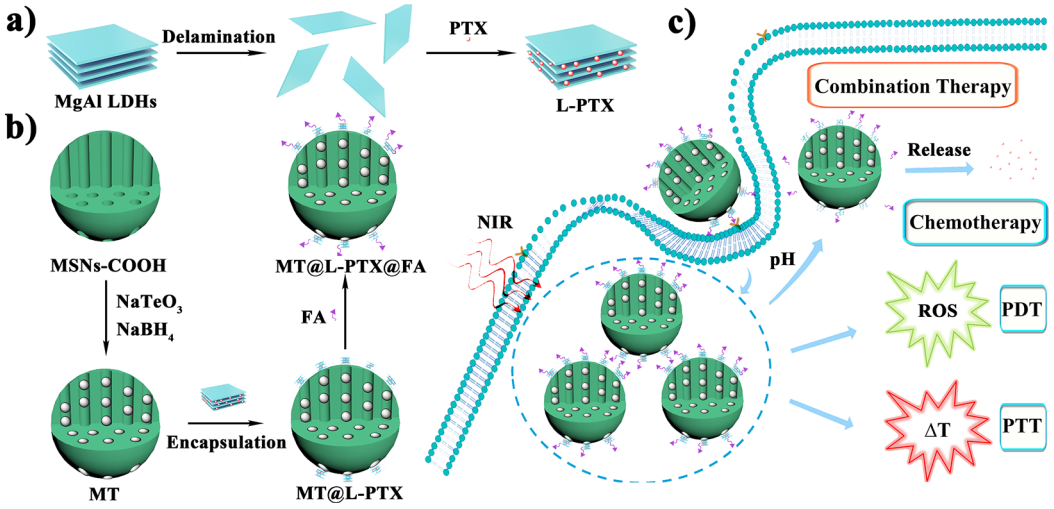

has recently been reported to show great potential as a phototherapeutic agent in cancer therapy.[27−30] For example, Te nanosheets have been synthesized via a facile liquid exfoliation method for photoacoustic imaging guided PDT.[31] Polysaccharide−protein complex modified Te nanorods have been used for chemo/PTT combination cancer therapy.[32] In particular, human serum albumin (HSA) has been utilized as a size-limited nanoreactor to generate Te nanodots (Te NDs), and certain synergistic anticancer efficacy was obtained since the synthesized ultrasmall size Te NDs exhibited PDT and PTT dual functions.[33] Thus, Te NDs with dual functions can be a good candidate for combinatorial therapy. Unfortunately, the nanodot size and homogeneity are the two most crucial factors to guarantee the efficiency and synergy of PDT and PTT,[33,34] and the cavity size of HSA is not a good candidate to control the proposed homogeneity.

In recent years, stimuli-responsive drug delivery systems (DDSs) based on mesoporous silica nanoparticles (MSNs) have drawn much attention due to the unique properties of MSNs such as stable porous structure, tunable pore size, good biocompatibility, and high specific surface area.[35−39] In particular, the pore entrance size of MSNs can be controlled precisely, which is just an ideal well-defined size-limited reaction space for the in situ formation of homogeneous ultrasmall Te NDs; thus, the aforementioned two most crucial factors to guarantee the efficiency and synergy of PDT and PTT from Te NDs could be achieved. Apart from providing reaction space, MSNs can also endow therapeutic agents with cancer cell targeting ability and precise release, in which MSNs serve as controlled nanocarriers to avoid the side effects resulting from the premature release of drugs.[40−42]

To avoid premature release and achieve targeted delivery, the gatekeepers of MSNs, which respond to the specific internal or external stimuli of cancer cells, play prominent and crucial roles. Layered double hydroxides (LDHs), consisting of positively charged brucite-type layers, are some of the prominent members of MSNs benefiting from their good biocompatibility, low cytotoxicity, pH-controlled degradation properties in acidic environments, and ease of surface modification.[43] Especially, LDHs not only can act as pH-controlled gatekeepers but also can act as nanocarriers themselves.[44] Therefore, the combination of Te ND in situ formed MSNs and drug-loaded LDHs gatekeepers can be a powerful stimuli-responsive DDS for targeted synergistic trimode combinatorial therapy.

As a proof of concept, in this study, a targeted nanosystem based on in situ formation of Te NDs in MSNs has been designed for chemo/PDT/PTT trimode combinatorial therapy (Scheme 1). As designed, Te NDs were grown in situ within the pores of carboxyl-functionalized MSNs (MSNs-COOH), giving Te ND-doped MSNs-COOH (MT). Subsequently, anticancer drug paclitaxel (PTX)-loaded MgAl LDHs (L-PTX) were adsorbed on the surface of MT by electrostatic interactions, yielding L-PTX gated MT (MT@L-PTX) to avoid the premature leakage of Te NDs. To endow the nanosystem with cancer selectivity, folic acid (FA) molecules, which have high affinity to the overexpressed FA receptor on the plasma membrane of most cancer cells, were covalently attached onto the surface of MT@L-PTX, giving FA modified MT@L-PTX (MT@L-PTX@FA). In this system, the in situ formed homogeneous Te NDs served as the phototherapeutic agent, converting the photon energy to reactive oxygen species (ROS) and heat under near-infrared (NIR) irradiation, causing damage to cancer cells. When the as-prepared MT@L-PTX@FA selectively entered into cancer cells, the low intracellular pH would dissolve MgAl LDHs to Mg^{2+} and Al^{3+}, thus leading to the release of PTX for chemotherapy. Meanwhile, upon NIR irradiation, Te NDs would convert the photon energy to ROS and heat for PDT and PTT, simultaneously. The results indicated that the chemo/PDT/PTT trimode combinatorial therapy was more efficient to kill cancer cells in comparison to either dual-mode combinatorial therapy or single therapy alone. The preliminary results reported here will shed new light on the future design and applications of nanosystems for synergistic combinatorial therapy.

EXPERIMENTAL SECTION

Reagents and Apparatus. Folic acid (FA), *N*-hydroxysuccinimide (NHS), 1-ethyl-3-(3-dimethylaminopropyl)carbodimide (EDC), tetraethoxysilane (TEOS), cetyltrimethylammonium bromide (CTAB), 3-aminopropyltrimethoxysilane (APTMS), 3-(triethoxysilyl)propylsuccinic anhydride (TPS), sodium dodecyl sulfate (SDS), rhodamine B (RhB), 3-[4,5-dimethylthialzol-2-yl]-2,5-diphenyltetrazolium bromide (MTT), paclitaxel (PTX), 1,3-diphenylisobenzofuran (DPBF), and 2,7-dichlorodihydrofluorescein

DOI: 10.1021/acs.inorgchem.8b02821
Inorg. Chem. XXXX, XXX, XXX−XXX

diacetate (DCFH-DA) were obtained from Sigma-Aldrich. All aqueous solutions were prepared with ultrapure Milli-Q water (ρ > 18.0 MΩ cm^{-1}). Human cervical cancer cells HeLa and human embryonic kidney cells 293T were maintained in Dulbecco's Modified Eagle's Medium (DMEM, Invitrogen) with 10 v/v% fetal bovine serum (FBS) and 1 v/v% penicillin/streptomycin (complete DMEM) in 5% CO_2 at 37 °C. Human liver carcinoma cells HepG2 and human normal liver cells HL7702 were cultured in 1640 medium containing 10% FBS and 1% penicillin/streptomycin (complete 1640) in 5% CO_2 at 37 °C.

X-ray diffraction (XRD) analysis was carried out with a D/Max2550VB+/PC X-ray diffractometer with Cu Kα radiation (λ 0.15406 nm), using an operating voltage and current of 40 kV and 30 mA, respectively. The composition of the products was determined by X-ray photoelectron spectroscopy (XPS, Thermo ESCALAB 250). The dynamic light scattering (DLS) and zeta potential were characterized using a zetasizer instrument (Nano ZS, Malvern Instruments, U.K.). The absorption and emission spectra were collected using a Shimadzu 1750 UV−vis spectrometer and an RF-5301 fluorescence spectrometer (Japan), respectively. Fourier transform infrared (FT-IR) spectra were obtained on a Brucher EQUINX55 FTIR spectrophotometer by a standard KBr disk method in the range 400−4000 cm^{-1}. A Quanta 200 environmental scanning electron microscope (SEM) was used to observe the morphologies of the obtained materials. High-resolution transmission electron microscope (HRTEM) images and the element mapping were recorded with a JEM-3010 transmission electron microscope operating at 200 kV. Specimens were prepared through dispersing the samples into alcohol via ultrasonic treatment and dropped on carbon−copper grids for observation. The nitrogen adsorption and desorption isotherms were measured at liquid N_2 temperature using a Quantachrom Autosorb-iQ instrument, after degassing samples for 12 h at 120 °C. Surface area was calculated according to the conventional Brunauer−Emmett−Teller (BET) method, and then the adsorption branches of the isotherms were used to calculate the pore parameters using the BJH method. Inductively coupled plasma mass spectrometry (ICP-MS, Agilent 7700X, Agilent Technologies, USA) was utilized to analyze the element concentration of nanomaterials. ^{1}H NMR and ^{13}C NMR spectra were recorded on a Bruker 500 AVANCE III spectrometer with chemical shifts reported in ppm at room temperature (500 MHz for ^{1}H NMR and 125 MHz for ^{13}C NMR, Germany). Mass spectrum (MS) was obtained with a Thermo Fisher LCQ Fleet mass spectrometer (USA). Cell culture was carried out in an incubator with a humidified atmosphere of 5% CO_2 at 37 °C. Cell toxicity tests were tested by a microplate reader (KHB ST-360). The confocal laser microscope data were acquired using a confocal fluorescence microscope (Nikon A1R).

All of the experiments were performed in compliance with the relevant laws and institutional guidelines and were approved by Northwest A&F University.

Synthesis of RhB Conjugated PTX (RhB-PTX). RhB-PTX was synthesized according to our previous work.[45] The synthesis procedure of RhB-PTX is shown in Figure S1 in the Supporting Information.

Synthesis of PTX-TES. PTX (100 mg, 0.12 mmol) and chlorotriethylsilane (TESCl) (19.4 mg, 0.13 mmol) were dissolved in pyridine at room temperature. The solution was stirred at 25 °C for 3 h and then diluted with ethyl acetate (EA; 50 mL) and washed with water (3 × 5 mL) and brine (3 × 5 mL). The organic solvent was dried over $MgSO_4$ and concentrated, and the residue was purified by silica gel column chromatography (petroleum ether (PE)/dichloromethane (DCM) 4/1 to 2/1) to afford PTX-TES as a white solid (yield 80%). The product was characterized by ^{1}H NMR (Figure S2). ^{1}H NMR (500 MHz, $CDCl_3$): δ 8.16−8.10 (m, 2H), 7.77−7.71 (m, 2H), 7.54 (m, 4H), 7.43−7.32 (m, 6H), 7.12 (d, J = 8.9 Hz, 1H), 6.32−6.21 (m, 2H), 5.71 (m, 2H), 5.02−4.93 (m, 1H), 4.70 (d, J = 2.1 Hz, 1H), 4.43 (t, J = 7.3 Hz, 1H), 4.32 (d, J = 8.4 Hz, 1H), 4.22 (d, J = 8.5 Hz, 1H), 3.83 (d, J = 7.1 Hz, 1H),2.62−2.46 (m, 5H), 2.23 (s, 2H), 2.19−2.12 (m, 1H), 2.04 (s, 1H), 1.89 (m, 5H), 1.78 (br, 1H), 1.69 (m, 3H), 1.31−1.19 (m, 5H), 1.14 (s, 3H), 0.86−0.75 (m, 9H), 0.53−0.35 (m, 6H).

Synthesis of RhB-PTX. A solution of PTX-TES (50 mg, 0.05 mmol) and DMAP (1.22 mg, 0.01 mmol) in DCM was treated with EDC (44.92 mg, 0.25 mmol) and RhB (119.75 mg, 0.25 mmol) for 18 h at room temperature. The mixture was then washed with H_2O (3 × 5 mL). The organic solvent was dried over $MgSO_4$ and concentrated. The resulting residue was purified by silica gel column chromatography (EA/hexanes (HEX) 1/2) to afford RhB-PTX-TES as a red solid (yield 60%). Next, tetrabutylammonium fluoride (Bu_4NF; 30 μL, 0.03 mmol) was added to a solution of RhB-PTX-TES (30 mg, 0.03 mmol) in tetrahydrofuran (THF) at room temperature and stirred for 2 h at room temperature. The solution was diluted with EA (100 mL) and washed with water (3 × 10 mL) and brine (3 × 10 mL). The organic solvent was dried over $MgSO_4$ and concentrated, and the residue was purified by silica gel column chromatography (EA/HEX = 3/2) to afford RhB-PTX as a red solid (yield 95%). The product was characterized by ^{1}H NMR, MS, fluorescence, and UV−vis spectra (Figures S3−S5). ^{1}H NMR (500 MHz, $CDCl_3$): δ 9.06 (d, J = 7.2 Hz, 1H), 8.18−8.13 (m, 2H), 8.09−7.99 (m, 3H), 7.76−7.56 (m, 4H), 7.51 (m, 7.1 Hz, 5H), 7.33 (m, 5H), 7.25 (s, 1H), 7.19 (dd, J = 7.4, 1.1 Hz, 1H), 7.10 (t, J = 7.4 Hz, 1H), 6.98 (d, J = 9.4 Hz, 1H), 6.76 (m, 3H), 6.69 (dd, J = 9.6, 2.4 Hz, 1H), 6.24 (s, 1H), 6.08 (s, 1H), 5.98 (t, J = 8.4 Hz, 1H), 5.58 (d, J = 7.1 Hz, 1H), 5.51 (t, J = 7.3 Hz, 1H), 5.40 (dd, J = 10.6, 7.0 Hz, 1H), 4.94 (d, J = 7.2 Hz, 1H), 4.76 (d, J = 8.5 Hz, 1H), 4.22 (d, J = 8.4 Hz, 1H), 4.11 (d, J = 8.4 Hz, 1H), 3.63−3.52 (m, 8H), 3.34−3.25 (m, 1H), 2.33 (s, 3H), 2.02 (s, 3H), 1.82 (s, 1H), 1.79−1.73 (m, 6H), 1.71 (m, 3H), 1.30 (t, J = 7.1 Hz, 12H), 1.10 (m, J = 15.6 Hz, 5H), 0.96 (m, J = 7.4 Hz, 3H). MS (RhB-PTX): calcd M for ($C_{75}H_{80}N_3O_{16}^+$) 1279.44, found 1279.06.

Preparation of MgAl Layered Double Hydroxides (MgAl LDHs). MgAl LDHs were prepared by coprecipitation and subsequent hydrothermal treatment.[46] $Mg(NO_3)_2{\cdot}6H_2O$ (0.56 g, 1.5 mmol) and $Al(NO_3)_3{\cdot}9H_2O$ (0.77 g, 3.0 mmol) were dissolved in 60 mL of water, and the solution mixture was titrated with NaOH solution (0.175 mol L^{-1}, 60 mL) to pH 10 ± 0.5 with vigorous stirring within 30 min, followed by treatment at 100 °C for 16 h under a N_2 atmosphere. The solid was centrifuged and washed with water. Finally, the solid was dried at room temperature under high vacuum.

Delamination of MgAl LDHs. The delamination of MgAl LDHs was performed according to the previously reported method.[47] Briefly, MgAl LDHs (1.0 g) were dispersed in 200 mL of formamide (0.05%, w/v) with magnetic stirring, and the resulting dispersion was sonicated until it became transparent to provide a 5 mg mL^{-1} formamide dispersion of MgAl LDH nanosheets.

Preparation of PTX-Loaded MgAl LDHs (L-PTX). A coassembly route was used to synthesize L-PTX.[48] Briefly, a 0.01 M SDS aqueous solution was prepared by dissolving SDS (0.34 g) in deionized water (120 mL). A solution of PTX in chloroform (1.0 g L^{-1}) was also prepared by dissolving PTX (120 mg) in chloroform (120 mL). The chloroform PTX solution was then added to the as-prepared SDS aqueous solution (0.01 M) with continuous stirring, and the resulting system was stirred under N_2 to allow for the evaporation of the chloroform to give a PTX-loaded micelle mixture. A 120 mL portion of the 5 mg mL^{-1} MgAl LDH dispersion was then added to the micelle mixture with continuous stirring. The suspension was centrifuged and washed sequentially with deionized water and anhydrous ethanol using a redispersion/centrifugation process. The resulting solid sample, denoted as L-PTX, was dried with a vacuum freeze-dryer overnight. The loading amount of PTX was measured by UV−vis spectroscopy at 250 nm.

The loading of RhB-PTX was according to the above-mentioned method and named as L- RhB-PTX.

Preparation of Carboxyl-Functionalized MSNs (MSNs-COOH). MSNs-COOH was synthesized according to a previous report with slight modification.[49] Briefly, 1.0 g of CTAB and 3.5 mL of sodium hydroxide (2.0 M) were dissolved into 480 mL of double-distilled water and heated to 80 °C in 30 min. Then, 5.0 g of TEOS was added dropwise and the mixture stirred vigorously for 2 h to

DOI: 10.1021/acs.inorgchem.8b02821
Inorg. Chem. XXXX, XXX, XXX−XXX

obtain MSNs. Next, 1 mL of TPS was dripped into the solution and further stirred at 80 °C for another 4 h. After that, the precipitant was collected by vacuum filtration and washed with double-distilled water and methanol for 6 times each, respectively. Finally, the sample was dried with a vacuum oven at 80 °C overnight to yield MSNs-COOH. The surfactant was removed by an extraction method as in a previous study. The crude product was refluxed with a solution composed of 7.0 mL of HCl (37.4 wt %) and 120.0 mL of methanol at 60 °C for 24 h.

Preparation of Tellurium Nanodot (Te-ND) Doped MSNs-COOH (MT). Te-NDs were synthesized using MSNs-COOH as a nanoreactor. A 200.0 mL portion of 5.0 mg mL^{-1} MSNs-COOH was added dropwise to 40.0 mL of 20.0 mM Na_2TeO_3 with stirring. Next, 16.0 mL of 100.0 mM $NaBH_4$ as the reductant was further added to the mixture. Then, the reduction reaction was performed in the mixture at 55 °C for 4 h with vigorous stirring, followed by the formation of Te-NDs. Subsequently, the precipitant was collected by centrifugation and purified through the dialysis against distilled water. Finally, the sample was dried with a vacuum freeze-dryer overnight to yield MT.

To obtain free Te NDs, MT was added to a solution of Na_2CO_3 (470 mg, 5 mL) and stirred at 60 °C for 16 h. Subsequently, the precipitant was washed three times by ultrapure water, collected by centrifugation, and dried with a vacuum freeze-dryer overnight to yield free Te NDs.

Preparation of L-PTX Gated MT (MT@L-PTX). To gate the pores of MSNs-COOH, MT and L-PTX were dispersed ultrasonically in formamide (0.05%, w/v) and stirred for 20 min. The solid MT@L-PTX was centrifuged, and washed with water.

L-RhB-PTX gated MT was fabricated according to the aforementioned method and denoted as MT@L-RhB-PTX.

Preparation of FA Conjugated MT@L-PTX (MT@L-PTX@FA). First, toluene (33 mL), methanol (1.6 mL), APTMS (0.25 mL), and MT@L-PTX (50 mg) were mixed rigorously for 6 h under N_2. The product was washed several times by centrifugation at 3500 rpm to remove excess APTMS in the suspension and dried with a vacuum freeze-dryer overnight to yield APTMS conjugated MT@L-PTX (MT@L-PTX-APTMS).[50] A mixture of FA (0.24 g), EDC (0.12 g), and NHS (0.08 g) in dimethyl sulfoxide (DMSO, 40 mL) was stirred for 0.5 h at room temperature. Then, MT@L-PTX-APTMS (0.20 g) was added. The resulting mixture was stirred for 24 h at room temperature. The product was dialyzed by SPECTRUM molecular porous membrane tubing (1000 Da), collected by centrifugation, and then dried with a vacuum freeze-dryer overnight to yield MT@L-PTX@FA.

FA conjugated L-RhB-PTX was fabricated according to the aforementioned method and denoted as MT@L- RhB-PTX@FA.

In Vitro PTX Release Kinetics. To determine the kinetics of PTX release from MT@L-PTX@FA, MT@L-PTX@FA (4 mg) was incubated in 2 mL of phosphate buffer solution (PBS, pH 5.8, 0.02 M), which contained a 1/1 (v/v) mixture of water and methanol to increase the solubility of PTX, for different periods of time. The supernatant was collected by centrifugation at predetermined time points. PTX release was determined by measuring the absorption intensity at 250 nm by a UV−vis spectrometer.

For comparison, the release profile of PTX from MT@L-PTX@FA in PBS (pH 7.4, 0.02 M) and 10% FBS was conducted by the same procedure.

Evaluation of ROS. A solution of DPBF (300 μM) in DMSO (500 μL) was added to a solution of MT@L-PTX@FA (0.125, 0.25, and 0.5 mg mL^{-1}) in PBS buffer (pH 5.8, 2 mL). The resulting solutions containing 1.5 mg MT@L-PTX@FA and 75 μM DPBF were photoirradiated with 785 nm irradiation (2 W cm^{-2}) for different periods of time. Changes in the UV−vis spectra of DPBF were recorded.

To distinguish the type of ROS, the electron spin resonance (ESR) technique was employed to monitor ROS signals from MT@L-PTX@FA upon 785 nm irradiation using 5,5-dimethyl-1-pyrroline *N*-oxide (DMPO) as the spin-trapping agent of superoxide radicals.[33] Spectra of spin-trapped superoxide radicals were acquired by mixing 5 μL of DMPO (500 mM) with 100 μL of MT@L-PTX@FA. Then the samples were irradiated at 785 nm at 2 W cm^{-2} for 5 min, followed by ESR analysis. The ESR spectrum of MT@L-PTX@FA in the presence of DMPO without irradiation was collected as a control.

Evaluation of Photothermal Effect and Photostability. To evaluate the photothermal effect of MT@L-PTX@FA, the solutions of MT@L-PTX@FA (2 mL) were irradiated (785 nm, 2 W cm^{-2}) for 5 min at different concentrations (0.5, 1, and 2 mg mL^{-1}) and the temperature was measured every 30 s using a digital thermometer. Further, the solutions of MT@L-PTX@FA (2 mg mL^{-1}, 2 mL) were irradiated (785 nm) under different light intensities (0.5, 1, and 2 W cm^{-2}) for 5 min and the temperature was measured using the same method.

To evaluate the photostability for temperature elevation, MT@L-PTX@FA (2 mg mL^{-1}, 2 mL) was subjected to 785 nm irradiation at 2 W cm^{-2} for 5 min and then cooled to room temperature. Afterward, an additional four irradiation/cooling cycles were repeated. During these cycles, the temperature was monitored.

Cell Imaging. HepG2 cells and HL7702 cells were used for cell imaging. Cells were seeded in 35 mm plastic-bottomed μ-dishes for 24 h. The medium was replaced with a fresh one. The cells were then incubated with free RhB-PTX (40 μM) and MT@L-RhB-PTX@FA (800 μg mL^{-1}) with equivalent PTX concentrations, respectively. After incubation for 4 h, the medium was removed and the cells were washed with PBS (pH 7.4) three times. To analyze the target ability of FA, HepG2 cells were first incubated with FA (100 μM) for 30 min. The cells were then incubated with MT@L-RhB-PTX@FA for 4 h. The red fluorescence of RhB-PTX was observed by a confocal scanning microscope (CLSM, Nikon A1R) with an excitation wavelength of 488 nm.

ROS Detection in Cells. HepG2 cells (1×10^5) were seeded in 35 mm plastic-bottomed μ-dishes for 24 h. The medium was replaced with a fresh one. Next, the cells were treated with MT@L-PTX@FA (800 μg mL^{-1}) for 4 h and irradiated by a NIR laser (785 nm, 2 W cm^{-2}) for 5 min irradiation. Then the medium containing 10 μM DCFH-DA was refreshed. After 20 min incubation, the cells were washed with PBS and then observed under a CLSM.

Flow Cytometry. For flow cytometry studies, HepG2 cells (1×10^6) were seeded in six-well culture plates and grown overnight. The cells were then treated with MT@L-RhB-PTX@FA for 0 h, 15 min, 30 min, 1 h, 2 h, and 4 h (for FA-preincubation groups, cells were first incubated with FA (100 μM) for 30 min). A single cell suspension was prepared consecutively by trypsinization, washing with PBS, and filtration through a nylon mesh filter (300 mesh). Then, the cells were analyzed using a flow cytometer (PE) for RhB.

Cytotoxicity Evaluation. HepG2 and HL7702 cells were cultured in complete 1640 medium in 5% CO_2 at 37 °C. HeLa and 293T cells were cultured in complete DMEM medium in 5% CO_2 at 37 °C. The relative cytotoxicities of MT@L-PTX@FA, MT@L, and free PTX were evaluated in vitro by MTT assays, respectively. The cells were seeded in 96-well plates at a density of 1×10^4 cells per well in 100 μL of complete medium. In particular, after 4 h of growth at 37 °C, HepG2 and HeLa cells incubated with MT@L-PTX@FA and MT@L were irradiated by a NIR laser (785 nm, 2 W cm^{-2}) for 5 min irradiation. Subsequently, all groups of cells were incubated for another 44 h. The cells were washed, and the fresh medium containing MTT (0.5 mg mL^{-1}) was added into each plate. The cells were incubated for another 4 h. After that, the medium containing MTT was removed and DMSO (100 μL) was added to each well to dissolve the formazan crystals. Finally, the plate was gently shaken for 10 min and the absorbance at 490 nm was recorded with a microplate reader.

RESULTS AND DISCUSSION

Synthesis and Characterization of MT@L-PTX@FA. MgAl LDHs, L-PTX, MSNs-COOH, MT, MT@L-PTX, and MT@L-PTX@FA were first prepared step by step as illustrated in Scheme 1, and their physical/chemical properties were characterized in detail. On one hand, MgAl LDHs were

DOI: 10.1021/acs.inorgchem.8b02821
Inorg. Chem. XXXX, XXX, XXX−XXX

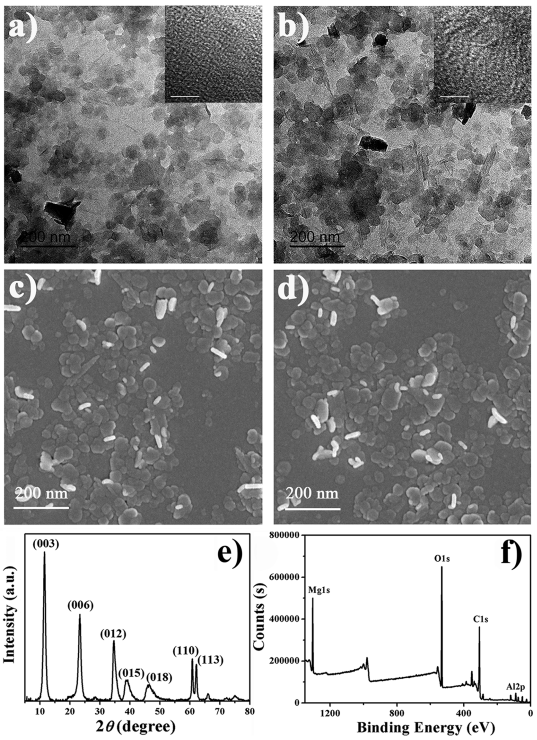

Figure 1. (a, b) HRTEM images of MgAl LDHs and L-PTX (scale bar 200 nm). (insets are images with high magnification; scale bar 5 nm). (c, d) SEM images of MgAl LDHs and L-PTX (scale bar 200 nm). (e) XRD pattern of MgAl LDHs; (f) XPS analysis of MgAl LDHs.

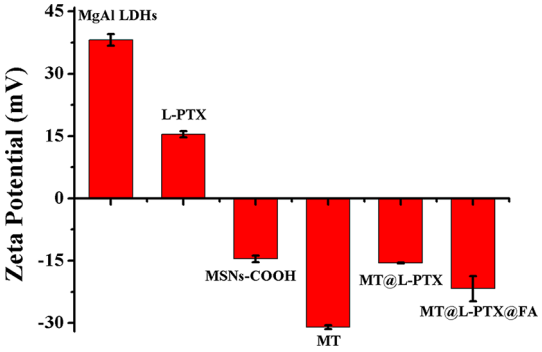

Figure 2. Zeta potential of MgAl LDHs, L-PTX, MSNs-COOH, MT, MT@L-PTX, and MT@L-PTX@FA.

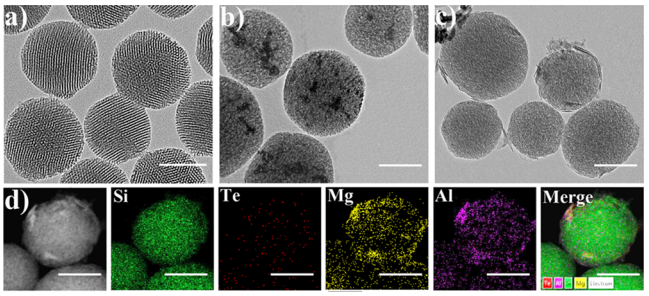

Figure 3. (a–c) HRTEM images of MSNs-COOH, MT and MT@L-PTX@FA. (d) TEM image and element mapping (Si, Te, Mg, Al, and merged image of Si, Te, Mg, Al) of MT@L-PTX@FA (scale bar 100 nm).

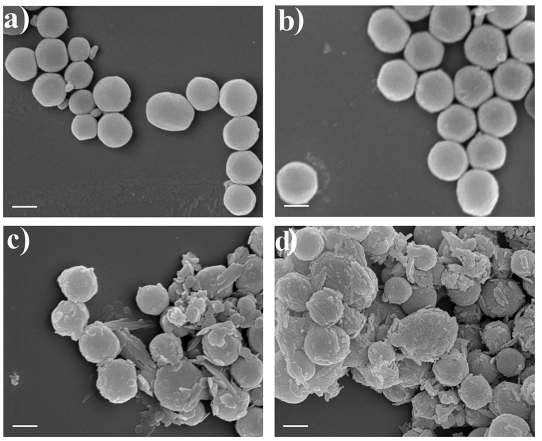

Figure 4. SEM images of (a) MSNs-COOH, (b) MT, (c) MT@L-PTX, and (d) MT@L-PTX@FA (scale bar 100 nm).

fabricated using a hydrothermal method according to the literature.[43] As shown in Figure 1, MgAl LDHs exhibited nearly hexagonal platelets with a lateral size, which is the typical morphology of LDH samples.[43] The typical XRD pattern and XPS also indicated the successful synthesis of MgAl LDHs.[43] Further, PTX was loaded into MgAl LDHs via a coassembly route,[48] in which PTX was initially incorporated into the micelles of the negatively charged surfactant SDS. The resulting negatively charged PTX-loaded micelles and the positively charged delaminated MgAl LDHs were then coassembled together obtaining L-PTX. HRTEM and SEM gave the morphology of L-PTX. The decreased zeta potential (from 38.1 to 15.4 mV) of L-PTX confirmed the intercalation of PTX-loaded micelles into MgAl LDHs (Figure 2). The PTX loading amount of the L-PTX was calculated to be 4.2% by UV–vis spectroscopy.

On the other hand, MSNs-COOH were first prepared by a sol–gel method,[49] and then Te-NDs were synthesized in situ using the pores of MSNs-COOH as nanoreactors yielding MT.[33] The successful fabrication of the nanomaterials was confirmed by HRTEM (Figure 3) and SEM (Figure 4) images, XRD (Figure 5a), XPS (Figure 5b,c), BET surface values (Figure 5d), pore volumes (Figure 5e), and the pore size (Figure 5f). HRTEM and SEM images revealed that Te-NDs were generated in situ in the pores of MSNs-COOH. The XRD pattern of MT exhibited the characteristic Bragg peaks at (011) and (102) facets that confirmed the generation of Te-NDs.[33] XPS also suggested the composition of Te^0 element. Moreover, BET surface values, pore volumes, and the pore size calculated from the N_2 adsorption–desorption isotherms for MT showed a significant decrease in comparison to that of MSNs-COOH, which is typical of mesoporous systems with filled pores, indicating that Te-NDs were generated in situ in the pores of MSNs-COOH. In addition, free Te NDs obtaining via the etching of MSNs showed a homogeneous diameter of about 3 nm, benefiting from the well-defined pore entrances of MSNs (Figure S6). Next, the as-prepared L-PTX nanosheets were adsorbed on the surface of MT spheres by electrostatic interactions to encapsulate the Te NDs inside the pores of the MSNs-COOH, giving MT@L-PTX. HRTEM images showed that, for the sample of MT@L-PTX, L-PTX nanosheets were randomly packed on the surface of MT spheres. The appearance of the Mg 1s peak component and the Al 2p peak component in the XPS of MT@L-PTX also

DOI: 10.1021/acs.inorgchem.8b02821
Inorg. Chem. XXXX, XXX, XXX–XXX

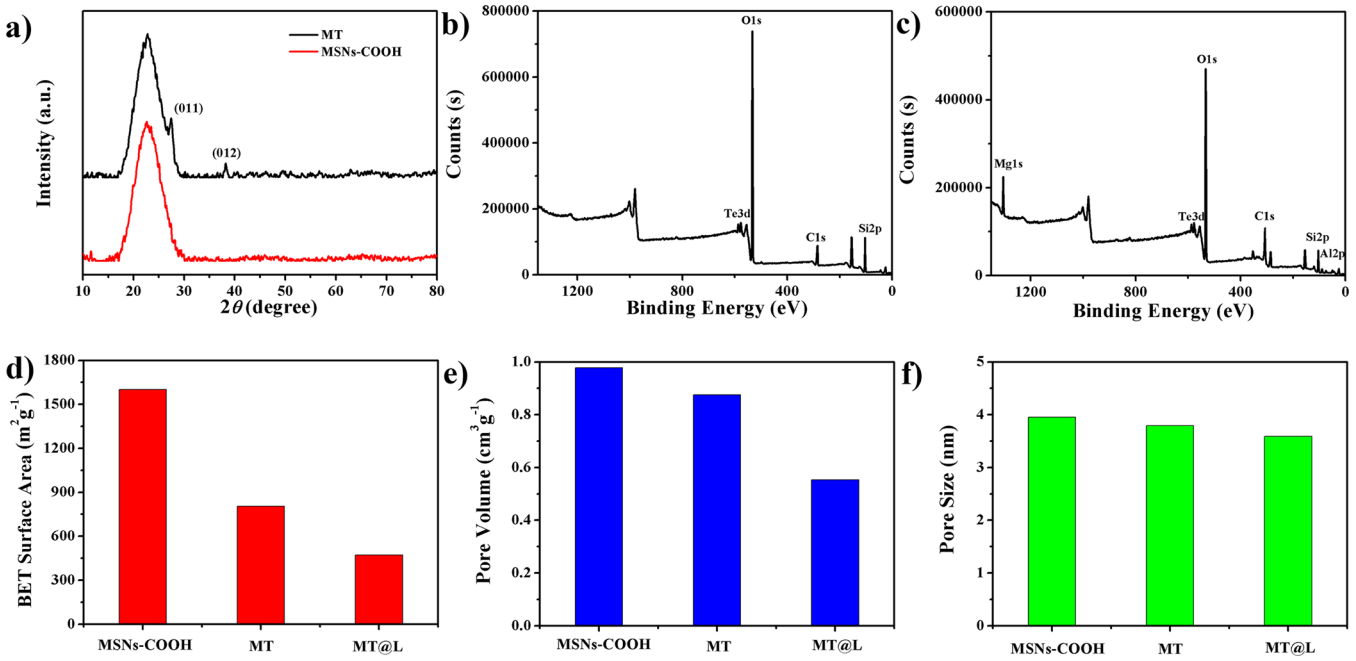

Figure 5. (a) XRD patterns of MSNs-COOH and MT. (b) XPS analysis of MT. (c) XPS analysis of MT@L. (d) BET surface areas of MSNs-COOH, MT, and MT@L. (e) Pore volumes of MSNs-COOH, MT, and MT@L. (f) Pore sizes of MSNs-COOH, MT, and MT@L.

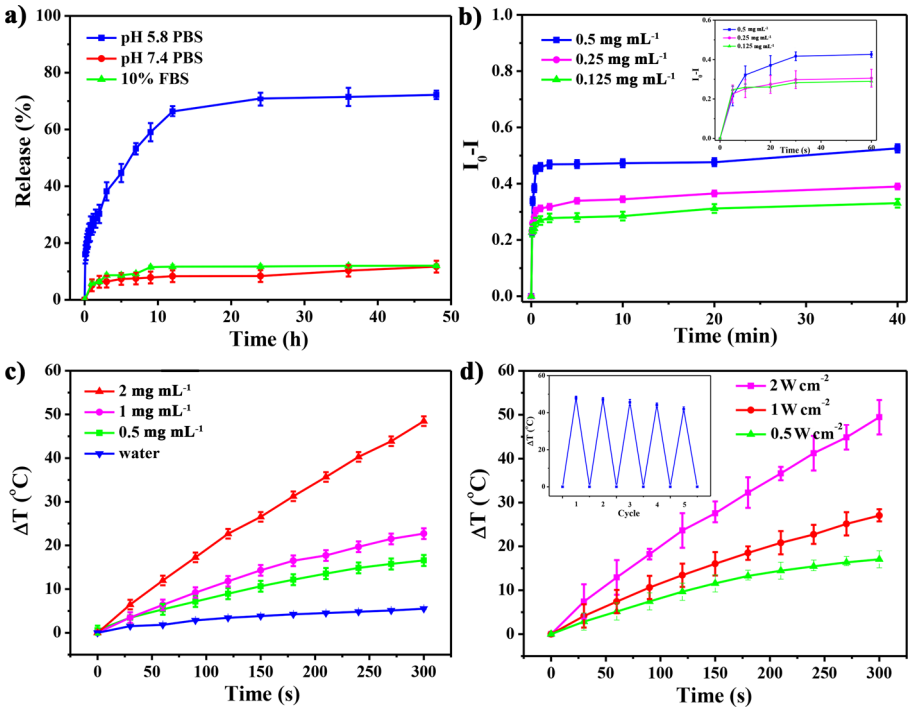

Figure 6. (a) Release kinetics of PTX from MT@L-PTX@FA in PBS (pH 5.8) and stability of MT@L-PTX@FA in PBS (pH 7.4) and 10% FBS. (b) Concentration-dependent ROS generation from MT@L-PTX@FA under 785 nm irradiation at 2 W cm^{-2} using DPBF as a probe. Inset: magnification of one segment. (c) Concentration-dependent temperature elevation of MT@L-PTX@FA under 785 nm irradiation at 2 W cm^{-2}. (d) Light-intensity-dependent temperature elevation of MT@L-PTX@FA (2 mg mL^{-1}) under 785 nm irradiation. Inset: temperature elevation of MT@L-PTX@FA (2 mg mL^{-1}) under five irradiation/cooling cycles.

confirmed the existence of the L-PTX coating. Moreover, the estimated weight percentage of L-PTX in MT@L-PTX obtained from ICP-MS was about 39.6% (Figure S7). Finally, FA molecules were conjugated onto MT@L-PTX, and the final nanosystem MT@L-PTX@FA was obtained (Figure S8 revealed that the hydrodynamic size of MT@L-PTX@FA obtained from DLS was about 250 nm). As shown in Figure S9, the FT-IR spectra of MT@L-PTX@FA exhibited additional absorption bands at 1639 and 1401 cm^{-1} in comparison with that of MT@L-PTX, which were assigned to the symmetrical ν_s(C═O) and asymmetric ν_{as}(C═O) vibrations of FA, respectively,[51] indicating the successful conjugation of FA.

DOI: 10.1021/acs.inorgchem.8b02821
Inorg. Chem. XXXX, XXX, XXX−XXX

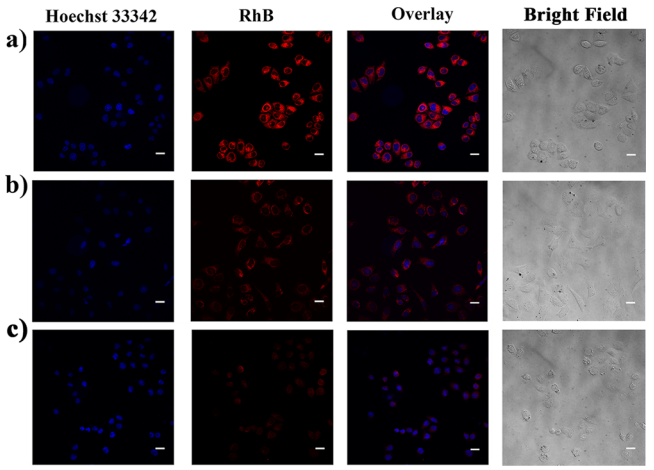

Figure 7. CLSM images of HepG2 cells incubated with MT@L-RhB-PTX@FA for 4 h: (a) without FA preincubation and (b) with FA preincubation, respectively. (c) HL7702 cells incubated with MT@L-RhB-PTX@FA for 4 h (scale bar 20 μm).

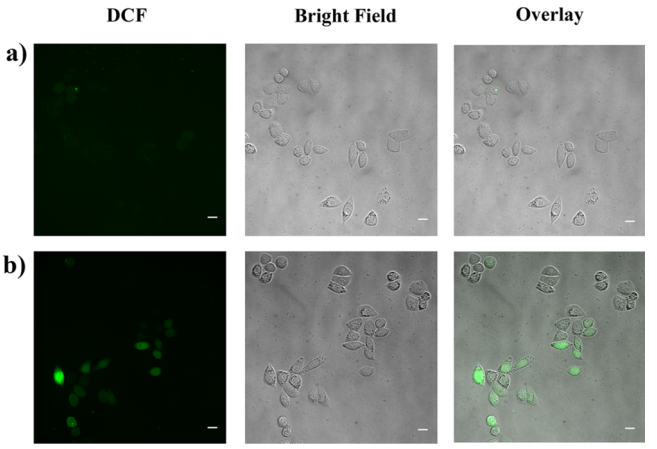

Figure 9. DCF fluorescence images in HepG2 cells treated with MT@L-RhB-PTX@FA under 785 nm irradiation (2 W cm^{-2}) for (a) 0 min and (b) 5 min (scale bar 20 μm).

In Vitro Drug Release of MT@L-PTX@FA. The feasibility of pH-triggered drug release of the nanosystem in vitro was then investigated. MT@L-PTX@FA was added into PBS (pH 5.8, 0.02 M), which contained a 1/1 (v/v) mixture of water and methanol to increase the solubility of PTX, and the release efficiency was evaluated by recording the absorbance at 250 nm. As shown in Figure 6a, approximately 70% PTX was released from MT@L-PTX@FA at pH 5.8, which mimics the acidic environment of tumor sites, because of the degradation of MgAl-LDHs. In comparison, MT@L-PTX@FA showed very high stability under physiological conditions of PBS (pH 7.4) and 10% FBS. Hence, MT@L-PTX@FA exhibited pH-responsive drug release.

ROS Generation, Photothermal Effect, and Photostability of MT@L-PTX@FA. To assess the capability of ROS generation of MT@L-PTX@FA, DPBF was employed as a probe molecule. The photo-oxidation of DPBF was monitored for 40 min under 785 nm light irradiation (2 W cm^{-2}). As shown in Figure 6b, in the presence of MT@L-PTX@FA, the DPBF absorption decreased continuously over the course of light irradiation, confirming the generation of ROS. In addition, MT@L-PTX@FA also exhibited a concentration dependent ROS generation. Further, the ESR technique was employed, indicating that the main type of ROS generated from MT@L-PTX@FA under irradiation was superoxide radicals (Figure S10).[33] These results indicate that this nanosystem has a good capacity for potential PDT.

We next proceeded to investigate the photothermal effect of MT@L-PTX@FA in vitro. As shown in Figure 6c,d, MT@L-PTX@FA had a concentration-dependent as well as light-intensity-dependent temperature increase under irradiation (785 nm), while water showed no significant temperature elevation. All of these results indicated that MT@L-PTX@FA

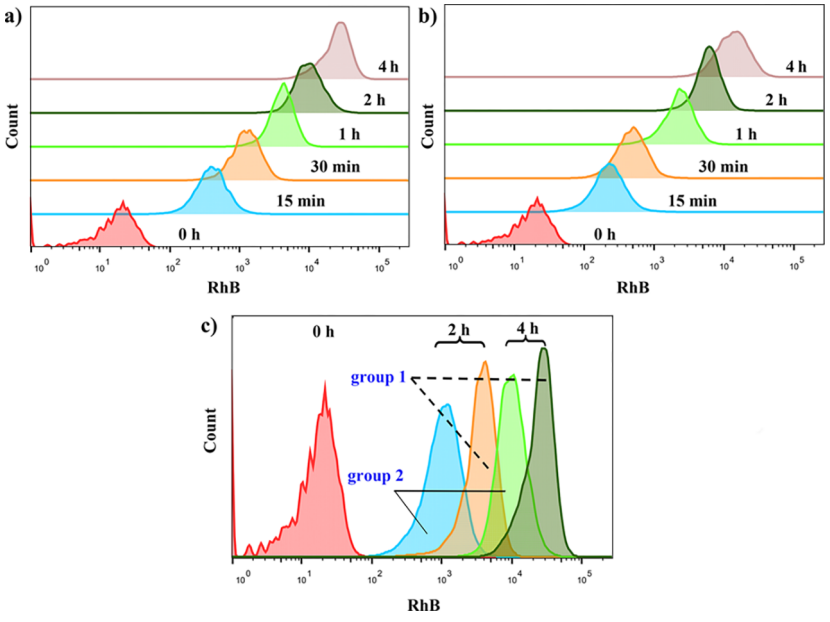

Figure 8. Flow cytometry analysis of HepG2 cells incubated with (a) MT@L-RhB-PTX@FA for 0 h, 15 min, 30 min, 1 h, 2 h, and 4 h, (b) RhB-PTX for 0 h, 15 min, 30 min, 1 h, 2 h, and 4 h, and (c) MT@L-RhB-PTX@FA for 0, 2, and 4 h (group 1, without FA preincubation; group 2, with FA preincubation).

DOI: 10.1021/acs.inorgchem.8b02821
Inorg. Chem. XXXX, XXX, XXX−XXX

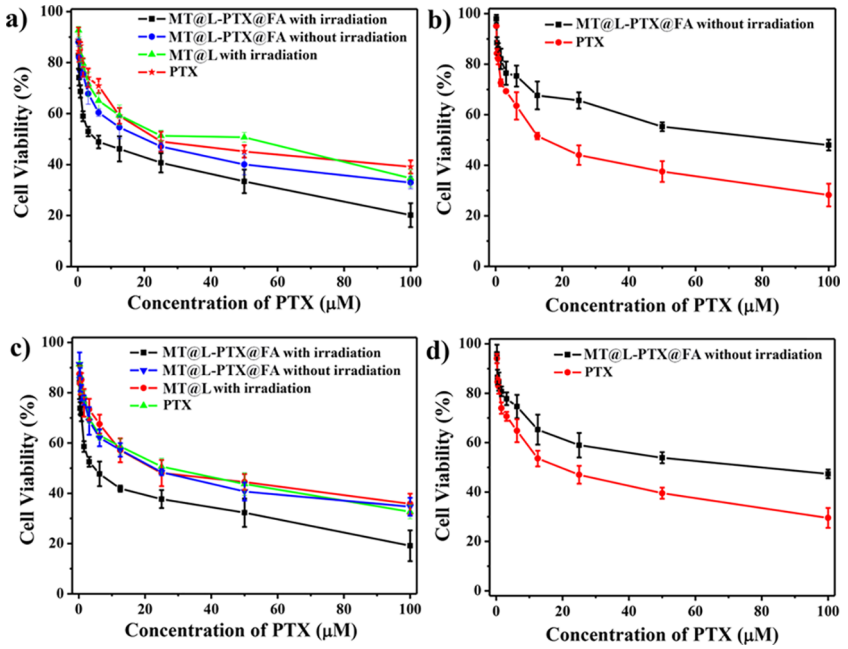

Figure 10. Cytotoxicity of MT@L-PTX@FA with or without irradiation, MT@L with irradiation, and free PTX at different concentrations on (a) HepG2 cells and (c) HeLa cells for 48 h. Cytotoxicity of MT@L-PTX@FA without irradiation and free PTX at different concentrations on (b) HL7702 cells and (d) 293T cells for 48 h.

had a strong ability to generate potent hyperthermia. To further confirm the photostability, we evaluated the ability of MT@L-PTX@FA to maintain temperature elevation under irradiation. The solutions of MT@L-PTX@FA suffered from 5 min irradiation (785 nm) at 2 W cm^{-2} and then were cooled to room temperature in the absence of irradiation for 5 min, followed by another four cycles of irradiation/cooling. As shown in the inset of Figure 6d, MT@L-PTX@FA had a temperature elevation of 47.0 °C after the first irradiation/cooling cycle and exhibited no significant change in temperature elevation after five cycles, suggesting that MT@L-PTX@FA had a good resistance to photobleaching.

Intracellular Imaging. These encouraging results in solution prompted us to evaluate the feasibility of MT@L-PTX@FA as an anticancer agent in cells. First, the selective cellular internalization of MT@L-PTX@FA was tested by cell imaging using CLSM and flow cytometry. RhB conjugated PTX (RhB-PTX) was used instead of PTX here (the synthesis procedure and characterizations of RhB-PTX are shown in the Supporting Information), and the corresponding nanosystem was denoted as MT@L-RhB-PTX@FA. As shown in Figure 7a, MT@L-RhB-PTX@FA showed obvious red fluorescence after 4 h incubation in human liver cancer cells HepG2 that was focused mainly in the cytoplasm, which was also stronger than that of free RhB-PTX (Figure S11a). In comparison, for HepG2 cells preincubated with FA (Figure 7b), a sharp decrease in fluorescence was observed. In addition, for human normal liver cells HL7702 incubated with MT@L-RhB-PTX@FA, an obvious decrease of fluorescence was also observed (Figure 7c). However, the fluorescence intensity of HL7702 cells incubated with free RhB-PTX was almost the same as that of HepG2 cells (Figure S11b). The results of flow cytometry were consistent with those of CLSM (Figure 8). All of these can be ascribed to the targeting ability of FA, which remarkably enhances the cancer cellular internalization of MT@L-RhB-PTX@FA in comparison with free RhB-PTX.

Thereafter, the ROS production of MT@L-RhB-PTX@FA was performed with HepG2 cells using DCFH-DA as a probe molecule. HepG2 cells were incubated with MT@L-RhB-PTX@FA (800 $\mu g\ mL^{-1}$) for 4 h and then with or without 785 nm light irradiation for 5 min. The cells were then stained with 10 μM DCFH-DA for 10 min. As shown in Figure 9, after light irradiation, green fluorescence generated from DCFH-DA can be seen clearly, indicating that MT@L-RhB-PTX@FA can be used as a promising candidate for PDT in living cells.

In Vitro Cytotoxicity. To further evaluate the anticancer efficacy of the nanosystem in vitro, an MTT assay was used to assess the cell viability after the cells were treated with MT@L-PTX@FA with and without light irradiation. In addition, cells treated with MT@L and free PTX were used as a comparison. As shown in Figure 10, the cell viabilities of HepG2 cells (Figure 10a) incubated with MT@L-PTX@FA with irradiation were much lower than those incubated with MT@L under the same conditions, MT@L-PTX@FA without irradiation, and free PTX, which was ascribed to the chemo/PDT/PTT trimode therapeutic synergy of as-prepared MT@L-PTX@FA. However, the cell viabilities of HL7702 cells (Figure 10b) incubated with MT@L-PTX@FA without irradiation were much higher than those incubated with free PTX. In addition, HepG2 cells and HL7702 cells incubated with free PTX exhibited similar cytotoxicities. These results indicate that MT@L-PTX@FA had a highly selective toxicity for cancer cells thanks to the targeting ability of FA but also showed enhanced therapeutic effects upon light irradiation inside cells based on chemo/PDT/PTT trimode combinatorial therapy. To provide further evidence, human cervical cancer cells HeLa (Figure 10c) and human embryonic kidney cells 293T (Figure 10d) were used to repeat the experiments and consistent results were obtained.

Moreover, the synergistic effect between PDT and PTT was verified using MT@L under irradiation. The ROS scavenger vitamin C (Vc) was used to scavenge intracellular ROS from

DOI: 10.1021/acs.inorgchem.8b02821
Inorg. Chem. XXXX, XXX, XXX−XXX

MT@L under irradiation and thus to inhibit photodynamic activity, while cells were temporarily incubated at ∼4 °C during irradiation to avoid photothermal damage.[29] As shown in Figure S12, in comparison with the group incubated with MT@L under irradiation, the relative cell viability of MT@L was increased in the presence of 10 mM Vc, indicating that their cytotoxicity from PTT alone was distinctly decreased in the absence of ROS. Moreover, at ∼4 °C incubation, much higher cell viability was observed, indicating a much lower cytotoxicity caused by PDT alone. Therefore, MT@L exhibited a synergistic effect between PDT and PTT.

CONCLUSIONS

In summary, a FA-functioned targeted nanosystem based on in situ formation of Te NDs in PTX-loaded MgAl LDH gated MSNs has been successfully synthesized. The obtained nanosystem MT@L-PTX@FA exhibited an efficient in vitro PDT and PTT activity as well as intracellular pH-responsive drug release. Moreover, MT@L-PTX@FA could target cancer cells due to the function of FA. In particular, cytotoxicity tests indicated that, under NIR irradiation, more efficient therapeutic effects could be achieved using MT@L-PTX@FA, benefiting from therapeutic synergy based on chemo/PDT/PTT trimode combinatorial therapy, which provides a general and promising platform for cancer therapy.

ASSOCIATED CONTENT

Supporting Information

The Supporting Information is available free of charge on the ACS Publications website at DOI: 10.1021/acs.inorgchem.8b02821.

NMR, MS, UV−vis, and FT-IR spectra, HRTEM images, ICP-MS analysis, DLS data, ESR spectroscopy,and cell imaging and cell viability data (PDF)

AUTHOR INFORMATION

Corresponding Authors

*E-mail for F.L.: liufengyu@dlut.edu.cn
*E-mail for S.S.: sunsg@nwsuaf.edu.cn.

ORCID

Yongqian Xu: 0000-0002-3778-7332
Shiguo Sun: 0000-0003-3135-8542

Notes

The authors declare no competing financial interest.

ACKNOWLEDGMENTS

This work was financially supported by the National Natural Science Foundation of China (Nos. U1803283, 21878249, 21472016, 21576042). The authors thank Life Science Research Core Services (LSRCS), Northwest A&F University, for help with characterizations including SEM, TEM, CLSM, and flow cytometry.

REFERENCES

(1) Yang, G. B.; Xu, L. G.; Chao, Y.; Xu, J.; Sun, X. Q.; Wu, Y. F.; Peng, R.; Liu, Z. Hollow MnO_2 as a tumor-microenvironment-responsive biodegradable nano-platform for combination therapy favoring antitumor immune responses. *Nat. Commun.* **2017**, *8*, 902.

(2) Wen, J.; Yang, K.; Liu, F.; Li, H.; Xu, Y.; Sun, S. Diverse gatekeepers for mesoporous silica nanoparticle based drug delivery systems. *Chem. Soc. Rev.* **2017**, *46*, 6024−6045.

(3) Shi, P.; Qu, K.; Wang, J.; Li, M.; Ren, J.; Qu, X. pH-responsive NIR enhanced drug release from gold nanocages possesses high potency against cancer cells. *Chem. Commun.* **2012**, *48*, 7640−7642.

(4) Lee, M. H.; Sharma, A.; Chang, M. J.; Lee, J.; Son, S.; Sessler, J. L.; Kang, C.; Kim, J. S. Fluorogenic reaction-based prodrug conjugates as targeted cancer theranostics. *Chem. Soc. Rev.* **2018**, *47*, 28−52.

(5) Xu, J.; He, F.; Cheng, Z.; Lv, R.; Dai, Y.; Gulzar, A.; Liu, B.; Bi, H.; Yang, D.; Gai, S.; Yang, P.; Lin, J. Yolk-structured upconversion nanoparticles with biodegradable silica shell for FRET sensing of drug release and imaging-guided chemotherapy. *Chem. Mater.* **2017**, *29*, 7615−7628.

(6) Renaud, J. P.; Chung, C. W.; Danielson, U. H.; Egner, U.; Hennig, M.; Hubbard, R. E.; Nar, H. Biophysics in drug discovery: impact, challenges and opportunities. *Nat. Rev. Drug Discovery* **2016**, *15*, 679.

(7) Yu, X.; Gong, L.; Zhang, J.; Zhao, Z.; Zhang, X.; Tan, W. Nanocarrier based on the assembly of protein and antisense oligonucleotide to combat multidrug resistance in tumor cells. *Sci. China: Chem.* **2017**, *60*, 1318−1323.

(8) Zhao, Z.; Meng, H.; Wang, N.; Donovan, M. J.; Fu, T.; You, M.; Chen, Z.; Zhang, X.; Tan, W. A controlled-release nanocarrier with extracellular pH value driven tumor targeting and translocation for drug delivery. *Angew. Chem., Int. Ed.* **2013**, *52*, 7487−7491.

(9) Liu, H. W.; Hu, X. X.; Li, K.; Liu, Y.; Rong, Q.; Zhu, L.; Yuan, L.; Qu, F. L.; Zhang, X. B.; Tan, W. A mitochondrial-targeted prodrug for NIR imaging guided and synergetic NIR photodynamic-chemo cancer therapy. *Chem. Sci.* **2017**, *8*, 7689−7695.

(10) Cai, H.; Shen, T.; Kirillov, A. M.; Zhang, Y.; Shan, C.; Li, X.; Liu, W.; Tang, Y. Self-assembled upconversion nanoparticle clusters for NIR-controlled drug release and synergistic therapy after conjugation with gold nanoparticles. *Inorg. Chem.* **2017**, *56*, 5295−5304.

(11) Fan, H.; Zhang, X.; Lu, Y. Recent advances in DNAzyme-based gene silencing. *Sci. China: Chem.* **2017**, *60*, 591−601.

(12) Sun, Q.; He, F.; Sun, C.; Wang, X.; Li, C.; Xu, J.; Yang, D.; Bi, H.; Gai, S.; Yang, P. Honeycomb-satellite structured pH/H_2O_2-responsive degradable nanoplatform for efficient photodynamic therapy and multimodal imaging. *ACS Appl. Mater. Interfaces* **2018**, *10*, 33901−33912.

(13) Zhu, H.; Cheng, P.; Chen, P.; Pu, K. Recent progress in the development of near-infrared organic photothermal and photodynamic nanotherapeutics. *Biomater. Sci.* **2018**, *6*, 746−765.

(14) Gai, S.; Yang, G.; Yang, P.; He, F.; Lin, J.; Jin, D.; Xing, B. Recent advances in functional nanomaterials for light−triggered cancer therapy. *Nano Today* **2018**, *19*, 146−187.

(15) Fan, H.; Yan, G.; Zhao, Z.; Hu, X.; Zhang, W.; Liu, H.; Fu, X.; Fu, T.; Zhang, X. B.; Tan, W. A smart photosensitizer−manganese dioxide nanosystem for enhanced photodynamic therapy by reducing glutathione levels in cancer cells. *Angew. Chem., Int. Ed.* **2016**, *55*, 5477−5482.

(16) Wang, X.; Tan, L. L.; Yang, Y. W. Controlled drug release systems based on mesoporous silica capped by gold nanoparticles. *Huaxue Xuebao* **2016**, *74*, 303−311.

(17) Dai, Y.; Xu, C.; Sun, X.; Chen, X. Nanoparticle design strategies for enhanced anticancer therapy by exploiting the tumour microenvironment. *Chem. Soc. Rev.* **2017**, *46*, 3830−3852.

(18) Zhou, J.; Yu, G.; Huang, F. Supramolecular chemotherapy based on host-guest molecular recognition: a novel strategy in the battle against cancer with a bright future. *Chem. Soc. Rev.* **2017**, *46*, 7021−7053.

(19) Zhang, Y.; Qu, Q.; Cao, X.; Zhao, Y. NIR-absorbing dye functionalized hollow mesoporous silica nanoparticles for combined photothermal-chemotherapy. *Chem. Commun.* **2017**, *53*, 12032−12035.

(20) Taratula, O.; Schumann, C.; Duong, T.; Taylor, K. L.; Taratula, O. Dendrimer-encapsulated naphthalocyanine as a single agent-based theranostic nanoplatform for near-infrared fluorescence imaging and

DOI: 10.1021/acs.inorgchem.8b02821
Inorg. Chem. XXXX, XXX, XXX−XXX

combinatorial anticancer phototherapy. *Nanoscale* **2015**, *7*, 3888−3902.
(21) Yuan, Y.; Liu, J.; Liu, B. Conjugated-Polyelectrolyte-Based Polyprodrug: Targeted and image-guided photodynamic and chemotherapy with on-demand drug release upon irradiation with a single light source. *Angew. Chem., Int. Ed.* **2014**, *53*, 7163−7168.
(22) Yang, D.; Yang, G.; Wang, X.; Lv, R.; Gai, S.; He, F.; Gulzar, A.; Yang, P. Y_2O_3:Yb,Er@mSiO_2−CuxS double-shelled hollow spheres for enhanced chemo-/photothermal anti-cancer therapy and dual-modal imaging. *Nanoscale* **2015**, *7*, 12180−12191.
(23) Zhang, Y. Y.; Yang, D.; Chen, H. Z.; Lim, W. Q.; Phua, F. S. Z.; An, G. H.; Yang, P. P.; Zhao, Y. L. Reduction-sensitive fluorescence enhanced polymeric prodrug nanoparticles for combinational photothermal-chemotherapy. *Biomaterials* **2018**, *163*, 14−24.
(24) Borghese, R.; Brucale, M.; Fortunato, G.; Lanzi, M.; Mezzi, A.; Valle, F.; Cavallini, M.; Zannoni, D. Extracellular production of tellurium nanoparticles by the photosynthetic bacterium Rhodobacter capsulatus (Reprinted from Journal of Hazardous Materials, vol 309, pg 202−209, 2016). *J. Hazard. Mater.* **2017**, *324*, 31−38.
(25) Baesman, S. A.; Bullen, T. D.; Dewald, J.; Zhang, D. H.; Curran, S.; Islam, F. S.; Beveridge, T. J.; Oremland, R. S. Formation of tellurium nanocrystals during anaerobic growth of bacteria that use te oxyanions as respiratory electron acceptors. *Appl. Environ. Microb.* **2007**, *73*, 2135−2143.
(26) He, Z.; Yang, Y.; Liu, J.-W.; Yu, S.-H. Emerging tellurium nanostructures: controllable synthesis and their applications. *Chem. Soc. Rev.* **2017**, *46*, 2732−2753.
(27) Cao, W.; Gu, Y.; Li, T.; Xu, H. Ultra-sensitive ROS-responsive tellurium-containing polymers. *Chem. Commun.* **2015**, *51*, 7069−7071.
(28) Li, F.; Li, T.; Cao, W.; Wang, L.; Xu, H. Near-infrared light stimuli-responsive synergistic therapy nanoplatforms based on the coordination of tellurium-containing block polymer and cisplatin for cancer treatment. *Biomaterials* **2017**, *133*, 208−218.
(29) Cao, W.; Gu, Y.; Meineck, M.; Li, T.; Xu, H. Tellurium-containing polymer micelles: competitive-ligand-regulated coordination responsive systems. *J. Am. Chem. Soc.* **2014**, *136*, 5132−5137.
(30) Pandey, S.; Talib, A.; Mukeshchand Thakur, M.; Shahnawaz Khan, M.; Bhaisare, M. L.; Gedda, G.; Wu, H.-F. Tellurium platinate nanowires for photothermal therapy of cancer cells. *J. Mater. Chem. B* **2016**, *4*, 3713−3720.
(31) Lin, Y.; Wu, Y.; Wang, R.; Tao, G.; Luo, P.-F.; Lin, X.; Huang, G.; Li, J.; Yang, H. H. Two-dimensional tellurium nanosheets for photoacoustic imaging-guided photodynamic therapy. *Chem. Commun.* **2018**, *54*, 8579−8582.
(32) Huang, W.; Huang, Y.; You, Y.; Nie, T.; Chen, T. High-yield synthesis of multifunctional tellurium nanorods to achieve simultaneous chemo-photothermal combination cancer therapy. *Adv. Funct. Mater.* **2017**, *27*, 1701388.
(33) Yang, T.; Ke, H. T.; Wang, Q. L.; Tang, Y. A.; Deng, Y. B.; Yang, H.; Yang, X. L.; Yang, P.; Ling, D. S.; Chen, C. Y.; Zhao, Y. L.; Wu, H.; Chen, H. B. Bifunctional tellurium nanodots for photoinduced synergistic cancer therapy. *ACS Nano* **2017**, *11*, 10012−10024.
(34) Jung, H. S.; Verwilst, P.; Sharma, A.; Shin, J.; Sessler, J. L.; Kim, J. S. Organic molecule-based photothermal agents: an expanding photothermal therapy universe. *Chem. Soc. Rev.* **2018**, *47*, 2280−2297.
(35) He, Q.; Shi, J. Mesoporous silica nanoparticle based nano drug delivery systems: synthesis, controlled drug release and delivery, pharmacokinetics and biocompatibility. *J. Mater. Chem.* **2011**, *21*, 5845−5855.
(36) Luo, Z.; Hu, Y.; Cai, K.; Ding, X.; Zhang, Q.; Li, M.; Ma, X.; Zhang, B.; Zeng, Y.; Li, P.; Li, J.; Liu, J.; Zhao, Y. Intracellular redox-activated anticancer drug delivery by functionalized hollow mesoporous silica nanoreservoirs with tumor specificity. *Biomaterials* **2014**, *35*, 7951−7962.
(37) Wen, J.; Yan, H.; Xia, P.; Xu, Y.; Li, H.; Sun, S. Mesoporous silica nanoparticles-assisted ruthenium(II) complexes for live cell staining. *Sci. China: Chem.* **2017**, *60*, 799−805.
(38) Tarn, D.; Xue, M.; Zink, J. I. pH-responsive dual cargo delivery from nesoporous silica nanoparticles with a metal-latched nanogate. *Inorg. Chem.* **2013**, *52*, 2044−2049.
(39) Yang, G.; Lv, R.; Gai, S.; Dai, Y.; He, F.; Yang, P. Multifunctional SiO_2@Gd_2O3:Yb/Tm hollow capsules: controllable synthesis and drug release properties. *Inorg. Chem.* **2014**, *53*, 10917−10927.
(40) Yuan, F.; Li, J. L.; Cheng, H.; Zeng, X.; Zhang, X. Z. A redox-responsive mesoporous silica based nanoplatform for in vitro tumor-specific fluorescence imaging and enhanced photodynamic therapy. *Biomater. Sci.* **2018**, *6*, 96−100.
(41) Wen, J.; Yang, K.; Xu, Y.; Li, H.; Liu, F.; Sun, S. Construction of a triple-stimuli-responsive system based on cerium oxide coated mesoporous silica nanoparticles. *Sci. Rep.* **2016**, *6*, 38931.
(42) Feng, R.; Shi, W.; Wang, D.; Wen, J.; Li, H.; Sun, S.; Xu, Y. Hierarchical self-assembly of squaraine and silica nanoparticle functionalized with cationic coordination sites for near infrared detection of ATP. *Sci. Rep.* **2017**, *7*, 43491.
(43) Zheng, Q.; Hao, Y.; Ye, P.; Guo, L.; Wu, H.; Guo, Q.; Jiang, J.; Fu, F.; Chen, G. A pH-responsive controlled release system using layered double hydroxide (LDH)-capped mesoporous silica nanoparticles. *J. Mater. Chem. B* **2013**, *1*, 1644−16488F.
(44) Wang, Z.; Ma, R.; Yan, L.; Chen, X.; Zhu, G. Combined chemotherapy and photodynamic therapy using a nanohybrid based on layered double hydroxides to conquer cisplatin resistance. *Chem. Commun.* **2015**, *51*, 11587−11590.
(45) Li, F. F.; Lu, J.; Liu, J.; Liang, C.; Wang, M. L.; Wang, L. Y.; Li, D. F.; Yao, H. Z.; Zhang, Q. L.; Wen, J.; Zhang, Z. K.; Li, J.; Lv, Q. X.; He, X. J.; Guo, B. S.; Guan, D. G.; Yu, Y. Y.; Dang, L.; Wu, X. H.; Li, Y. S.; Chen, G. F.; Jiang, F.; Sun, S. G.; Zhang, B. T.; Lu, A. P.; Zhang, G. A water-soluble nucleolin aptamer-paclitaxel conjugate for tumor-specific targeting in ovarian cancer. *Nat. Commun.* **2017**, *8*, 1390.
(46) Zheng, Q. S.; Hao, Y. L.; Ye, P. R.; Guo, L. Q.; Wu, H. Y.; Guo, Q. Q.; Jiang, J. Z.; Fu, F. F.; Chen, G. N. A pH-responsive controlled release system using layered double hydroxide (LDH)-capped mesoporous silica nanoparticles. *J. Mater. Chem. B* **2013**, *1*, 1644−1648.
(47) Wu, Q. L.; Olafsen, A.; Vistad, O. B.; Roots, J.; Norby, P. Delamination and restacking of a layered double hydroxide with nitrate as counter anion. *J. Mater. Chem.* **2005**, *15*, 4695−4700.
(48) Wu, X. W.; Li, H. P.; Song, S.; Zhang, R. J.; Hou, W. G. Facile synthesis of camptothecin intercalated layered double hydroxide nanohybrids via a coassembly route. *Int. J. Pharm.* **2013**, *454*, 453−461.
(49) Zhang, B. L.; Luo, Z.; Liu, J. J.; Ding, X. W.; Li, J. H.; Cai, K. Y. Cytochrome c end-capped mesoporous silica nanoparticles as redox-responsive drug delivery vehicles for liver tumor-targeted triplex therapy in vitro and in vivo. *J. Controlled Release* **2014**, *192*, 192−201.
(50) Chen, T. J.; Cheng, T. H.; Hung, Y. C.; Lin, K. T.; Liu, G. C.; Wang, Y. M. Targeted folic acid-PEG nanoparticles for noninvasive imaging of folate receptor by MRI. *J. Biomed. Mater. Res., Part A* **2008**, *87A*, 165−175.
(51) Li, C. Y.; Liang, R. Z.; Tian, R.; Guan, S. Y.; Yan, D. P.; Luo, J. Y.; Wei, M.; Evans, D. G.; Duan, X. A targeted agent with intercalation structure for cancer near-infrared imaging and photothermal therapy. *RSC Adv.* **2016**, *6*, 16608−16614.

DOI: 10.1021/acs.inorgchem.8b02821
Inorg. Chem. XXXX, XXX, XXX−XXX